



An Adaptive Multiresolution Ultra-weak Discontinuous Galerkin Method for Nonlinear Schrödinger Equations

Zhanjing Tao¹ · Juntao Huang² · Yuan Liu³ · Wei Guo⁴ · Yingda Cheng⁵

Received: 30 June 2020 / Revised: 11 September 2020 / Accepted: 30 October 2020 /
Published online: 25 January 2021
© Shanghai University 2021

Abstract

This paper develops a high-order adaptive scheme for solving nonlinear Schrödinger equations. The solutions to such equations often exhibit solitary wave and local structures, which make adaptivity essential in improving the simulation efficiency. Our scheme uses the ultra-weak discontinuous Galerkin (DG) formulation and belongs to the framework of adaptive multiresolution schemes. Various numerical experiments are presented to demonstrate the excellent capability of capturing the soliton waves and the blow-up phenomenon.

Keywords Multiresolution · Sparse grid · Ultra-weak discontinuous Galerkin method · Schrödinger equation · Adaptivity

Mathematics Subject Classification 65M60

✉ Juntao Huang
huangj75@msu.edu

Zhanjing Tao
zjtiao@jlu.edu.cn

Yuan Liu
liu@math.wichita.edu

Wei Guo
weimath.guo@ttu.edu

Yingda Cheng
ycheng@msu.edu

¹ School of Mathematics, Jilin University, Jilin 130012, China

² Department of Mathematics, Michigan State University, East Lansing, MI 48824, USA

³ Department of Mathematics, Statistics and Physics, Wichita State University, Wichita, KS 67260, USA

⁴ Department of Mathematics and Statistics, Texas Tech University, Lubbock, TX 70409, USA

⁵ Department of Mathematics, Department of Computational Mathematics, Science and Engineering, Michigan State University, East Lansing, MI 48824, USA

1 Introduction

In this paper, we develop a class of adaptive multiresolution ultra-weak discontinuous Galerkin (DG) method to solve the nonlinear Schrödinger (NLS) equations in a d -dimensional space

$$iu_t + \Delta u + f(|u|^2)u = 0, \quad (1)$$

where u is a complex function, and f is a smooth nonlinear real function. The Schrödinger equation is of fundamental importance in quantum mechanics, reaching out to many important applications describing the physical phenomena including nonlinear optics, semiconductor electronics, quantum fluids and plasma physics [10, 32, 43]. Numerical methods for solving the NLS equations have been investigated extensively, including finite difference [5, 24, 36, 38, 40], finite element [8, 16, 25, 45], and spectral methods [14, 34, 39], to name a few. In this paper, we consider the DG method [12, 13, 35], which is a class of finite element methods using piecewise polynomial spaces for the numerical solutions and the test functions. The last several decades have seen tremendous developments of DG methods in approximating partial differential equations (PDEs) in large part due to their distinguished advantages in handling geometry, boundary conditions and accommodating adaptivity. Various types of DG methods have been proposed to compute the NLS equations. In [45], an LDG method using alternating fluxes was developed with L^2 stability and the sub-optimal error estimates. An LDG method with various numerical fluxes was analyzed in [27]. An analysis of the LDG method for the NLS equation with the wave operator was carried out in [17]. The direct DG (DDG) method was applied to the Schrödinger equation in [29], and the optimal accuracy was further established in [28]. In [44], a hybridized DG (HDG) method was applied to a linear Schrödinger equation. In this paper, we use the ultra-weak DG method [9], which is a class of DG methods use repeated integration by parts for calculating higher order derivatives. The ultra-weak DG schemes include the DDG and interior penalty DG methods, and have been investigated in [7, 8] for convergence and superconvergence.

The solutions to NLS equations present solitary waves, blow-up and other localized structures. Therefore, benefits of adaptivity in simulations are self-evident [6, 26, 37]. In this paper, we consider the adaptive multiresolution approach [15, 19, 21]. By exploring the inherent mesh hierarchy and the associated nestedness of the polynomial approximation spaces, multiresolution analysis (MRA) [30] is able to accelerate the computation and avoid the need for a posteriori error indicators. MRA is closely related to popular sparse grid methods [3] for solving high-dimensional problems. It is also related to the adaptive mesh refinement (AMR) technique [2, 4], which adjusts the computational grid adaptively to track small scale features of the underlying problems and improves computational efficiency. As a continuation of our previous research on adaptive multiresolution (also called adaptive sparse grid) DG methods [19–22], this paper develops an adaptive multiresolution ultra-weak DG solver for NLS equation (1) and the coupled NLS equations. First, the Alpert's multiwavelets are employed as the DG bases in the weak formulation, and then the interpolatory multiwavelets are introduced for efficiently computing nonlinear source which has been successfully applied to nonlinear hyperbolic conservation laws [21] and Hamilton-Jacobi equations [20]. We refer the readers to [19, 21] for more details on the background of adaptive multiresolution DG methods. Numerical experiments verify the accuracy of the methods. In particular, the adaptive scheme is demonstrated to capture the moving solitons and also the blow-up phenomenon very well.

The rest of the paper is organized as follows. In Sect. 2, we review Alpert’s multiwavelets. Section 3 describes the numerical schemes. Section 4 contains numerical examples. We make conclusions in Sect. 5.

2 MRA and Multiwavelets

In this section, we briefly review the fundamentals of MRA of DG approximation spaces and the associated multiwavelets. Two classes of multiwavelets, namely the L^2 orthonormal Alpert’s multiwavelets [1] and the interpolatory multiwavelets [41], are used to construct our ultra-weak DG scheme. We also introduce a set of key notations used throughout the paper by following [42].

Alpert’s multiwavelets [1] have been employed to develop a class of sparse grid DG methods for solving high dimensional PDEs [18, 42]. Considering a unit sized interval $\Omega = [0, 1]$ for simplicity, we define a set of nested grids $\Omega_0, \Omega_1, \dots$, for which the n -th level grid Ω_n consists of 2^n uniform cells

$$I_n^j = (2^{-n}j, 2^{-n}(j + 1)], \quad j = 0, \dots, 2^n - 1.$$

Denote $I_{-1} = [0, 1]$. The piecewise polynomial space of degree at most $k \geq 1$ on grid Ω_n for $n \geq 0$ is denoted by

$$V_n^k := \{v : v \in P^k(I_n^j), \forall j = 0, \dots, 2^n - 1\}. \tag{2}$$

Observing the nested structure

$$V_0^k \subset V_1^k \subset V_2^k \subset V_3^k \subset \dots,$$

we can define the multiwavelet subspace $W_n^k, n = 1, 2, \dots$ as the orthogonal complement of V_{n-1}^k in V_n^k with respect to the L^2 inner product on $[0, 1]$, i.e.,

$$V_{n-1}^k \oplus W_n^k = V_n^k, \quad W_n^k \perp V_{n-1}^k.$$

By letting $W_0^k := V_0^k$, we obtain a hierarchical decomposition $V_n^k = \bigoplus_{0 \leq l \leq n} W_l^k$, i.e., an MRA of space V_n^k . A set of orthonormal basis can be defined on W_l^k as follows. When $l = 0$, the basis $v_{i,0}^0(x), i = 0, \dots, k$ are the normalized shifted Legendre polynomials in $[0, 1]$. When $l > 0$, the Alpert’s orthonormal multiwavelets [1] are employed as the bases and denoted by

$$v_{i,j}^j(x), \quad i = 0, \dots, k, \quad j = 0, \dots, 2^{l-1} - 1.$$

We then follow a tensor-product approach to construct the hierarchical finite element space in multi-dimensional space. Denote $\mathbf{l} = (l_1, \dots, l_d) \in \mathbb{N}_0^d$ as the mesh level in a multivariate sense, where \mathbb{N}_0 denotes the set of nonnegative integers, we can define the tensor-product mesh grid as $\Omega_{\mathbf{l}} = \Omega_{l_1} \otimes \dots \otimes \Omega_{l_d}$ and the corresponding mesh size $h_{\mathbf{l}} = (h_{l_1}, \dots, h_{l_d})$. Based on the grid $\Omega_{\mathbf{l}}$, we denote $I_{\mathbf{l}}^{\mathbf{j}} = \{\mathbf{x} : x_m \in (h_m j_m, h_m(j_m + 1)), m = 1, \dots, d\}$ as an elementary cell, and

$$V_{\mathbf{l}}^k := \{v : v \in Q^k(I_{\mathbf{l}}^{\mathbf{j}}), \mathbf{0} \leq \mathbf{j} \leq 2^{\mathbf{l}} - \mathbf{1}\} = V_{l_1, x_1}^k \times \dots \times V_{l_d, x_d}^k$$

as the tensor-product piecewise polynomial space, where $Q^k(I_1^j)$ represents the collection of polynomials with a degree of up to k in each dimension on cell I_1^j . If we use equal mesh refinement of size $h_N = 2^{-N}$ in each coordinate direction, the grid and space will be denoted by Ω_N and \mathbf{V}_N^k , respectively. Based on a tensor-product construction, the multi-dimensional increment space can be defined as

$$\mathbf{W}_1^k = W_{l_1, x_1}^k \times \cdots \times W_{l_d, x_d}^k.$$

The basis functions in case of multi-dimensions are defined as

$$v_{\mathbf{i}, \mathbf{l}}^{\mathbf{j}}(\mathbf{x}) := \prod_{m=1}^d v_{l_m, l_m}^{j_m}(x_m) \tag{3}$$

for $\mathbf{l} \in \mathbb{N}_0^d$, $\mathbf{j} \in B_1 := \{\mathbf{j} \in \mathbb{N}_0^d : \mathbf{0} \leq \mathbf{j} \leq \max(2^{l-1} - \mathbf{1}, \mathbf{0})\}$ and $\mathbf{1} \leq \mathbf{i} \leq \mathbf{k} + \mathbf{1}$.

By introducing the standard norms for the multi-index

$$\|\cdot\|_1 := \sum_{m=1}^d l_m, \quad \|\cdot\|_\infty := \max_{1 \leq m \leq d} l_m,$$

together with the same component-wise arithmetic operations and relations as defined in [42], we achieve the decomposition

$$\mathbf{V}_N^k = \bigoplus_{\substack{\|\cdot\|_\infty \leq N \\ \mathbf{l} \in \mathbb{N}_0^d}} \mathbf{W}_1^k. \tag{4}$$

Further, by a standard truncation of \mathbf{V}_N^k [18, 42], we obtain the sparse grid space

$$\hat{\mathbf{V}}_N^k = \bigoplus_{\substack{\|\cdot\|_1 \leq N \\ \mathbf{l} \in \mathbb{N}_0^d}} \mathbf{W}_1^k \subset \mathbf{V}_N^k. \tag{5}$$

We skip the details about the property of the space, but refer the readers to [18, 42]. In Sect. 3, we will describe the adaptive scheme that adapts a subspace of \mathbf{V}_N^k according to the numerical solution, hence offering more flexibility and efficiency.

Alpert’s multiwavelets described above are associated with the L^2 projection operator. For nonlinear source terms, we use the interpolatory multiwavelets based on Lagrange interpolations introduced in [41]. For details, we refer readers to [21, 41].

3 Adaptive Multiresolution DG Scheme

In this section, we present the adaptive multiresolution ultra-weak DG scheme for solving the NLS equation (1). We consider periodic boundary conditions for simplicity, while the method can be adapted to other non-periodic boundary conditions.

For illustrative purposes, we first introduce some basis notations about jumps and averages for piecewise functions defined on a grid Ω_N . Denote by Γ the union of the boundaries for all the elements in the partition Ω_N . The jump and average of $q \in L^2(\Gamma)$ and $\mathbf{q} \in [L^2(\Gamma)]^d$ are defined as follows. Suppose e is an edge shared by elements T^+ and T^- , we define the unit normal vectors \mathbf{n}^+ and \mathbf{n}^- on e pointing exterior to T^+ and T^- . Then,

$$\begin{aligned}
 [q] &= q^- \mathbf{n}^- + q^+ \mathbf{n}^+, & \{q\} &= \frac{1}{2}(q^- + q^+), \\
 [\mathbf{q}] &= \mathbf{q}^- \cdot \mathbf{n}^- + \mathbf{q}^+ \cdot \mathbf{n}^+, & \{\mathbf{q}\} &= \frac{1}{2}(\mathbf{q}^- + \mathbf{q}^+).
 \end{aligned}$$

For any subspace \mathbf{V} of \mathbf{V}_N^k , define the corresponding complex-valued finite element space

$$\mathbb{V} := \{v = v_1 + iv_2 : v_1, v_2 \in \mathbf{V}\}. \tag{6}$$

The semi-discrete ultra-weak DG scheme [8] for (1) is defined below. We are searching for $u_h \in \mathbb{V}$ such that for any test function $\phi_h \in \mathbb{V}$,

$$i \int_{\Omega} (u_h)_t \phi_h \, dx + \int_{\Omega} u_h \nabla^2 \phi_h \, dx - \sum_{e \in \Gamma} \int_e \hat{u}_h [\nabla \phi_h] \, ds + \sum_{e \in \Gamma} \int_e \widetilde{\nabla u_h} \cdot [\phi_h] \, ds + \int_{\Omega} f(|u_h|^2) u_h \phi_h \, dx = 0. \tag{7}$$

We take the following numerical fluxes:

$$\widetilde{\nabla u_h} = \{\nabla u_h\} + \alpha_1 [\nabla u_h] \mathbf{e} + \beta_1 [u_h], \quad \hat{u}_h = \{u_h\} + \alpha_2 [u_h] \cdot \mathbf{e} + \beta_2 [\nabla u_h]. \tag{8}$$

Here, $\alpha_1, \alpha_2, \beta_1$, and β_2 are prescribed complex numbers that may depend on the mesh size h and $\mathbf{e} = (1, \dots, 1) \in \mathbb{R}^d$. In this work, we numerically test two types of numerical fluxes. The first one is the alternating flux corresponding to $\alpha_1 = \frac{1}{2}, \alpha_2 = -\frac{1}{2}$ and $\beta_1 = \beta_2 = 0$. The second one is a dissipative numerical flux [8] with $\alpha_1 = \frac{1}{2}, \alpha_2 = -\frac{1}{2}, \beta_1 = 1 - i, \beta_2 = 1 + i$.

To efficiently calculate the nonlinear term $\int_{\Omega} f(|u_h|^2) u_h \phi_h \, dx$ in (7), the multiresolution Lagrange interpolation is applied [21, 41], i.e., we modified the weak formulation of ultra-weak DG as follows. We are searching for $u_h \in \mathbb{V}$ such that for any test function $\phi_h \in \mathbb{V}$,

$$\begin{aligned}
 i \int_{\Omega} (u_h)_t \phi_h \, dx + \int_{\Omega} u_h \nabla^2 \phi_h \, dx - \sum_{e \in \Gamma} \int_e \hat{u}_h [\nabla \phi_h] \, ds + \sum_{e \in \Gamma} \int_e \widetilde{\nabla u_h} \cdot [\phi_h] \, ds \\
 + \int_{\Omega} \mathcal{I}_h(f(|u_h|^2) u_h) \phi_h \, dx = 0.
 \end{aligned} \tag{9}$$

To preserve the accuracy of the original DG scheme (7), Lagrange interpolation of the same order must be applied in (9). For details, see the argument in [11, 21, 23]. By applying interpolation, the unidirectional principle and fast algorithm described in [21] can be employed to further improve efficiency. In numerical experiments, we also consider the coupled nonlinear Schrödinger equations in a one-dimensional space

$$iu_t + i\alpha u_x + u_{xx} + \beta u + \kappa v + f(|u|^2, |v|^2)u = 0, \tag{10a}$$

$$iv_t - i\alpha v_x + v_{xx} - \beta u + \kappa v + g(|u|^2, |v|^2)v = 0, \tag{10b}$$

where u and v are complex functions, f and g are smooth nonlinear real functions, and α, β, κ are real constants. We use the same DG scheme for solving the coupled NLS equation (10) except that the first order derivatives u_x and v_x are treated by the standard DG scheme with upwind numerical fluxes. The details are omitted here for brevity.

For time discretization, we employ the third-order implicit-explicit (IMEX) Runge-Kutta (RK) scheme [33] to advance the semi-discrete scheme (9). Specifically, the second derivative term u_{xx} is treated implicitly to avoid the severe CFL time constraint, while the nonlinear source $f(|u|^2)u$ is treated explicitly for efficiency. The adaptive procedure follows the technique developed in [20, 21] to determine the space \mathbf{V} that evolves dynamically

over time. The only difference is that the first-order Euler forward and Euler backward schemes are applied for the prediction. The main idea is that based on the distinguished properties of multiwavelets, we keep track of multiwavelet coefficients, i.e., L^2 norms of u_h , as an error indicator for refining and coarsening, aiming to efficiently capture the solitons or singular solutions of (1). We also remark that other types of time discretizations, e.g., exponential time differencing (ETD) or Krylov implicit integration factor (IIF) methods, could also be applied here. The efficiencies of different types of time stepping remain to be investigated.

4 Numerical Examples

In this section, we perform numerical experiments to validate the performance of our scheme. We consider the NLS equation (1) in 1D and 2D, and the coupled NLS equation (10) in 1D, with a computational domain of $[0, 1]^d$ with $d = 1, 2$. We employ the third order IMEX RK scheme in [33]. The CFL number is to be 0.1, i.e., $\Delta t = 0.1\Delta x$, unless otherwise stated. All adaptive calculations are obtained by $k = 3$. DoF = $\dim(\mathbf{V})$ refers to the number of Alpert’s multiwavelets basis function with respect to the adaptive grids.

4.1 Accuracy Test for NLS Equation

Example 1 We start with the accuracy test for the NLS equation on the domain $[0, 1]^d$:

$$iu_t + \Delta u + |u|^2u + |u|^4u = 0 \tag{11}$$

with periodic boundary conditions. The exact solution is

$$u(x, t) = \exp\left(i\left(2\pi \sum_{i=1}^d x_i - \omega t\right)\right) \tag{12}$$

with $\omega = 4d\pi^2 - 2$.

We first test the accuracy of the sparse grid methods in a 2D space. The results obtained by considering $k = 1, 2, 3$ are presented in Table 1. To ensure time accuracy, we take $\Delta t = 0.1\Delta x^{4/3}$ for $k = 3$. As expected, the average convergence order is between k and $k + 1$.

We then test the accuracy of adaptive method in 2D in Table 2. We observe that it takes much less DoF with higher-order polynomial degrees than lower-order ones.

We also show the comparison on the error vs. the CPU time for adaptive, sparse and full grid DG methods with $k = 2$ in Fig. 1. From the results, it is evident that the adaptive multiresolution method is the most efficient among the three methods in this 2D example. The sparse grid method outperforms the full grid method since the solution is smooth in this example and the sparse grid space $\hat{\mathbf{V}}_N^K$ ensures comparable accuracy to the full grid space \mathbf{V}_N^K with reduced DoFs.

Next, we compare the performance of our numerical scheme with the alternating (conservative) and dissipative numerical fluxes. The time history of the L^2 -error with different values of polynomial degrees k and error tolerance ϵ is shown in Fig. 2. Note that the adaptive scheme with dissipative flux and $k = 1$ does not converge because the

Table 1 Example 1, accuracy test for NLS equation, $d = 2$, sparse grid, $t = 0.1$

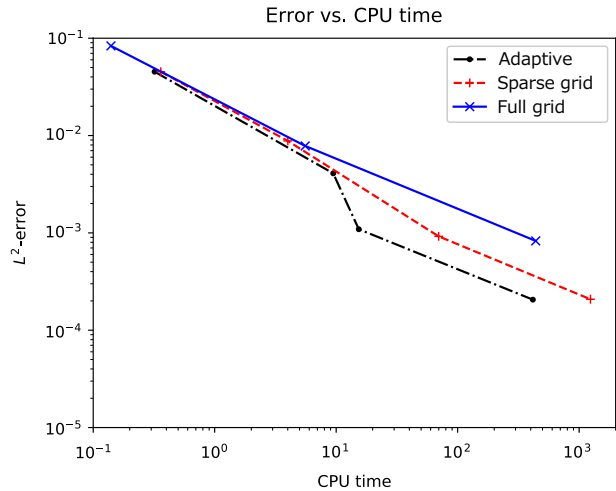
	N	Real part		Imaginary part	
		L^2 -error	Order	L^2 -error	Order
$k = 1$	5	2.82×10^{-1}	–	2.90×10^{-1}	–
	6	1.28×10^{-1}	1.15	1.35×10^{-1}	1.11
	7	1.90×10^{-2}	2.74	1.90×10^{-2}	2.83
	8	5.37×10^{-3}	1.82	5.27×10^{-3}	1.85
	9	1.13×10^{-3}	2.25	1.13×10^{-3}	2.22
$k = 2$	3	3.20×10^{-2}	–	4.33×10^{-2}	–
	4	7.91×10^{-3}	2.02	1.43×10^{-2}	1.60
	5	7.74×10^{-4}	3.35	7.77×10^{-4}	4.20
	6	1.88×10^{-4}	2.04	2.66×10^{-4}	1.55
	7	1.46×10^{-5}	3.68	1.47×10^{-5}	4.18
$k = 3$	3	9.82×10^{-3}	–	2.67×10^{-2}	–
	4	1.96×10^{-4}	5.64	2.29×10^{-4}	6.87
	5	2.05×10^{-5}	3.26	1.46×10^{-5}	3.97
	6	2.60×10^{-6}	2.98	9.40×10^{-7}	3.95
	7	5.99×10^{-8}	5.44	5.89×10^{-8}	4.00

Table 2 Example 1, accuracy test for NLS equation, $d = 2$. Adaptive. $t = 0.1$

ϵ	DoF	Real part of u			Imaginary part of u			
		L^2 -error	R_{DoF}	R_ϵ	L^2 -error	R_{DoF}	R_ϵ	
$k = 1$	1×10^{-1}	192	9.33×10^{-1}	–	–	9.59×10^{-1}	–	–
	1×10^{-2}	960	9.39×10^{-2}	1.43	1.00	9.25×10^{-2}	1.45	1.02
	1×10^{-3}	1 792	2.33×10^{-2}	2.23	0.61	2.29×10^{-2}	2.23	0.61
	1×10^{-4}	7 168	4.80×10^{-3}	1.14	0.69	4.78×10^{-3}	1.13	0.68
$k = 2$	1×10^{-1}	108	7.93×10^{-2}	–	–	8.68×10^{-2}	–	–
	1×10^{-2}	432	1.01×10^{-2}	1.49	0.89	9.60×10^{-3}	1.59	0.96
	1×10^{-3}	720	1.10×10^{-3}	4.35	0.96	1.11×10^{-3}	4.23	0.94
	1×10^{-4}	1 800	2.06×10^{-4}	1.82	0.73	2.99×10^{-4}	1.43	0.57
$k = 3$	1×10^{-2}	320	1.43×10^{-2}	–	–	2.86×10^{-2}	–	–
	1×10^{-3}	512	2.81×10^{-3}	3.46	0.71	2.81×10^{-3}	4.93	1.01
	1×10^{-4}	896	3.08×10^{-4}	3.95	0.96	3.07×10^{-4}	3.96	0.96
	1×10^{-5}	1 984	3.63×10^{-5}	2.69	0.93	3.63×10^{-5}	2.69	0.93

corresponding full grid DG is not consistent. In general, the two kind of numerical fluxes has the similar magnitude of errors. Since the conservative numerical flux performs better in regular DG [8], we will consider the conservative numerical flux in the following examples.

Fig. 1 Example 1: L^2 -error vs. CPU time for adaptive, sparse and full grid ultra-weak DG methods. $d = 2, t = 0.1, k = 2$



4.2 NLS Equation in 1D

Example 2 In this example, we show the soliton propagation of the NLS equation (1) in the domain $[0, 1]$:

$$iu_t + \frac{1}{M^2}u_{xx} + 2|u|^2u = 0 \tag{13}$$

with the initial conditions corresponding to the single soliton [45]

$$u(x, 0) = \operatorname{sech}(X - x_0) \exp(2i(X - x_0)) \tag{14}$$

and the double soliton [45]

$$u(x, 0) = \sum_{j=1}^2 \operatorname{sech}(X - x_j) \exp\left(\frac{1}{2}ic_j(X - x_j)\right) \tag{15}$$

with $X = M(x - \frac{1}{2})$. Here the parameters are taken as $M = 50, x_0 = 0, x_1 = -10, x_2 = 10, c_1 = 4$ and $c_2 = -4$.

The numerical solutions and the active elements for the single soliton (14) are shown in Fig. 3. We observe that the envelope or the modulus $|u|$ are captured by our adaptive scheme quite well. The active elements are also moving with the wave peak.

The numerical solutions and the active elements for double solitons (15) are shown in Fig. 4. The two waves propagate in opposite directions and collide at $t = 2.5$. After that, the two waves separate. Such behaviors are accurately captured by our numerical simulations. Moreover, our numerical solution does not generate symmetric active elements, which is due to the fact that the ultra-weak DG in full grid does not preserve the symmetry exactly.

Example 3 In this example, we consider the bound state solution of the equation [45]

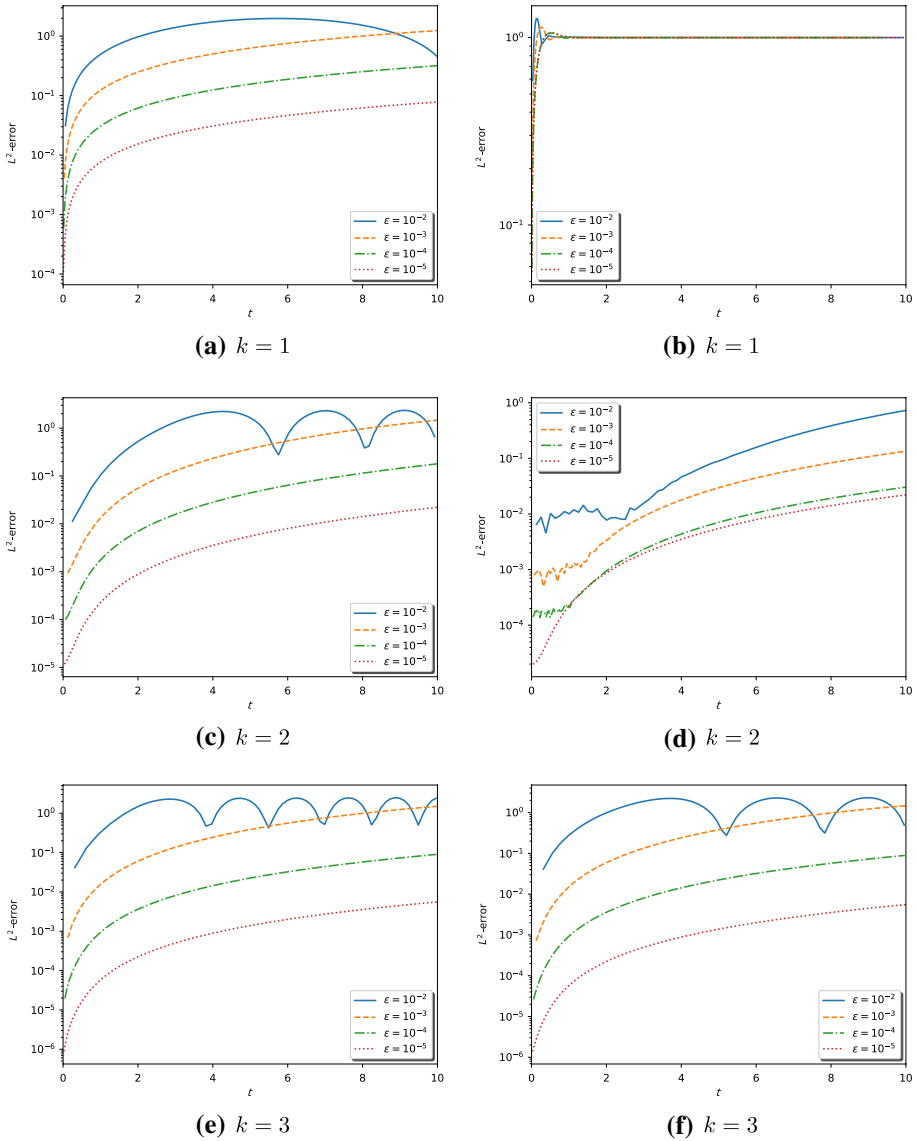


Fig. 2 Example 1: L^2 -error vs time. $d = 1, t = 10. N = 8$ and $\eta = \epsilon/10$. Left: conservative numerical flux; right: dissipative numerical flux

$$iu_t + \frac{1}{M^2}u_{xx} + \beta|u|^2u = 0 \tag{16}$$

with an initial condition of

$$u(x, 0) = \operatorname{sech} X, \tag{17}$$

where $X = M(x - 0.5), M = 30$.

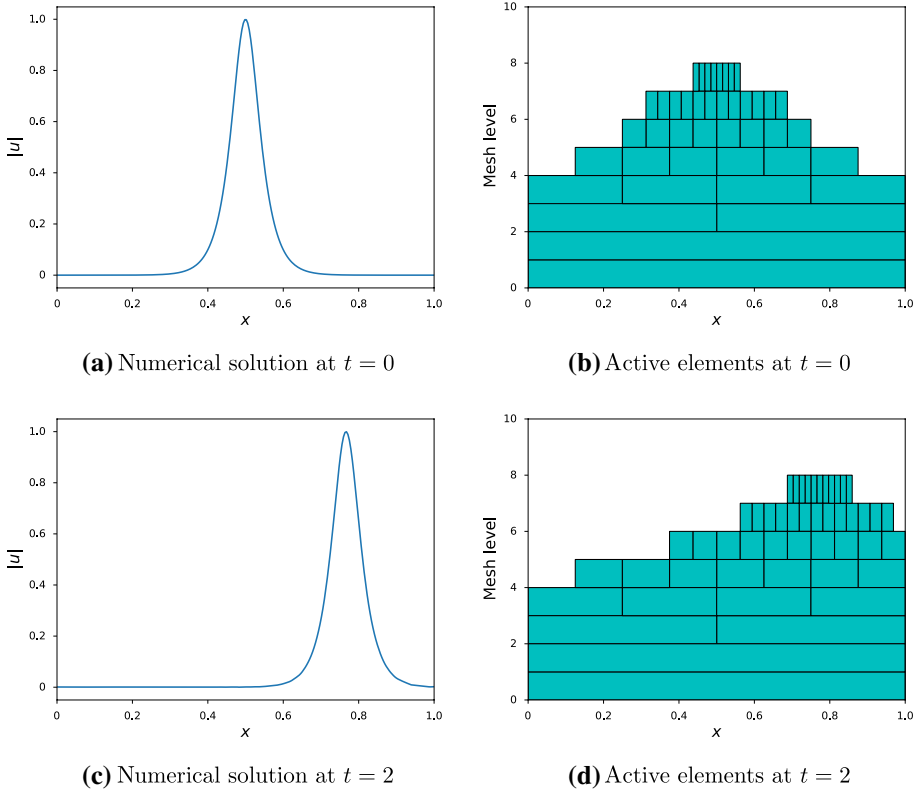


Fig. 3 Example 2: 1D NLS equation, single soliton. Left: numerical solutions; right: active elements. $t = 0$ and 2. $N = 8$, $\epsilon = 10^{-4}$, $\eta = 10^{-5}$

When $\beta = 2L^2$, it will produce a bound state of L solitons. The theoretical solution for a bound state of solitons is known [31]. If $L \geq 3$, small narrow structures will develop in the solution which require high mesh resolution to capture. Clearly, using a uniform mesh is far from being optimal due to such a highly localized structure. We present the numerical solutions and active elements of the bound state of solitons with $L = 3, 4, 5$ in Figs. 5, 6 and 7. The multiscale structure of the solutions is accurately captured by our adaptive method.

4.3 Coupled NLS Equation in 1D

Example 4 We show an accuracy test for the coupled NLS equation [45]

$$\begin{cases} iu_t + i\frac{\alpha}{M}u_x + \frac{1}{2M^2}u_{xx} + (|u|^2 + \beta|v|^2)u = 0, \\ iv_t - i\frac{\alpha}{M}v_x + \frac{1}{2M^2}v_{xx} + (\beta|u|^2 + |v|^2)v = 0 \end{cases} \quad (18)$$

with the soliton solution

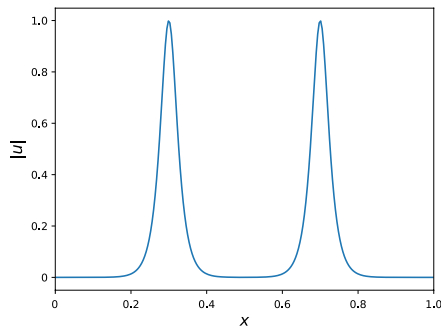
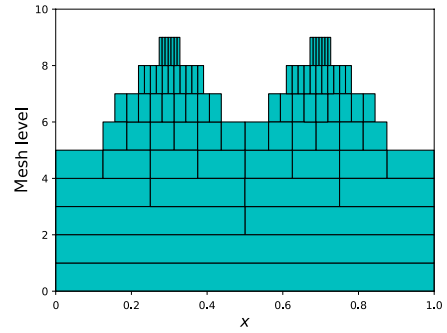
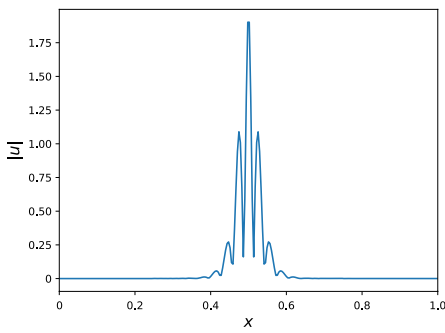
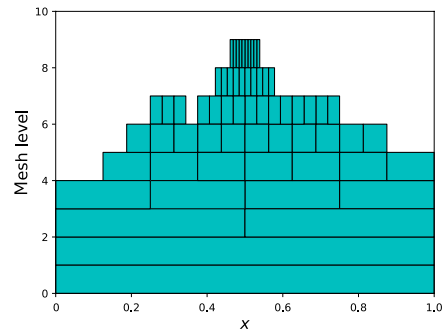
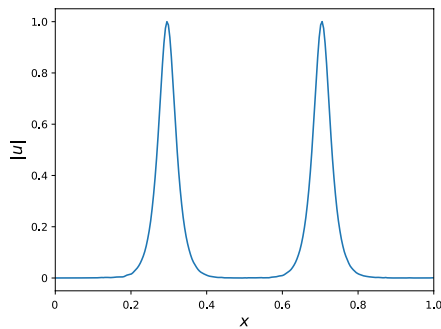
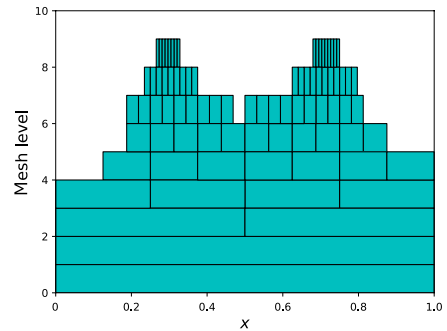
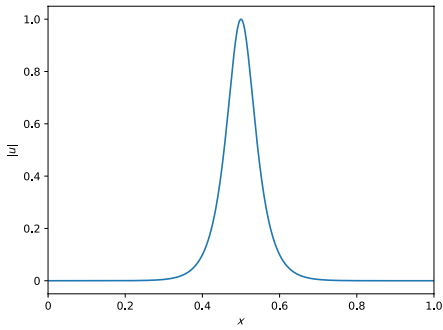
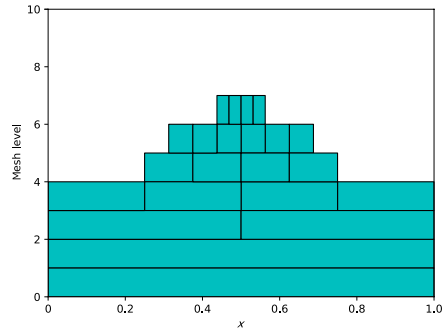
(a) Numerical solution at $t = 0$ (b) Active elements at $t = 0$ (c) Numerical solution at $t = 2.5$ (d) Active elements at $t = 2.5$ (e) Numerical solution at $t = 5$ (f) Active elements at $t = 5$

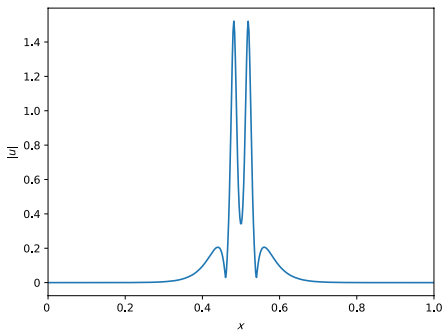
Fig. 4 Example 2: 1D NLS equation, double soliton. Left: numerical solutions; right: active elements. $t = 0, 2.5$ and 5 . $N = 8$, $\epsilon = 10^{-4}$, $\eta = 10^{-5}$



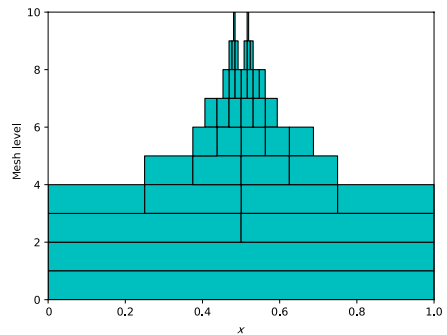
(a) Numerical solution at $t = 0$



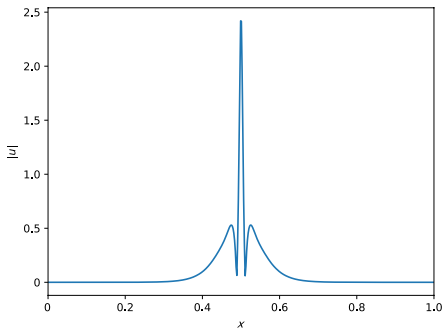
(b) Active elements at $t = 0$



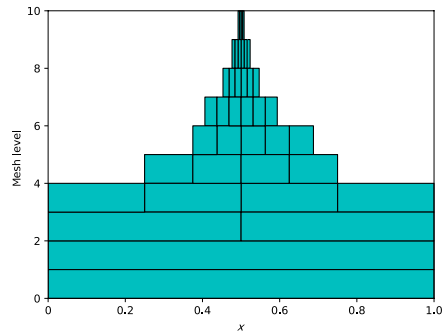
(c) Numerical solution at $t = 0.4$



(d) Active elements at $t = 0.4$



(e) Numerical solution at $t = 0.6$



(f) Active elements at $t = 0.6$

Fig. 5 Example 3: bound state solution of solitons with $L = 3$. Left: numerical solutions; right: active elements. $t = 0, 0.4$ and 0.6 . $N = 9, k = 3, \epsilon = 10^{-4}$ and $\eta = 10^{-5}$

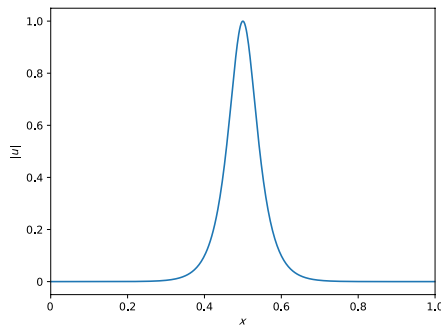
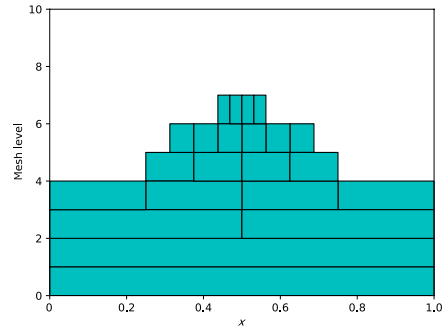
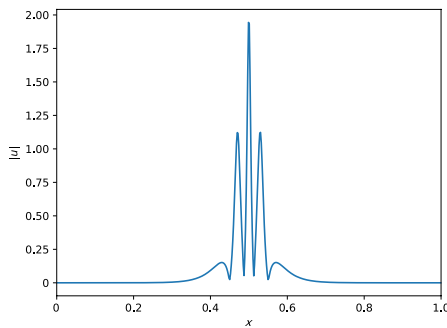
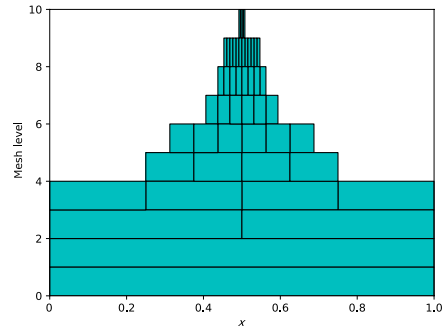
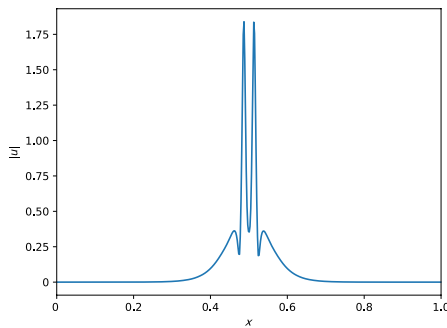
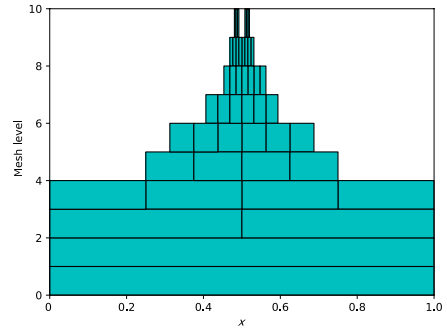
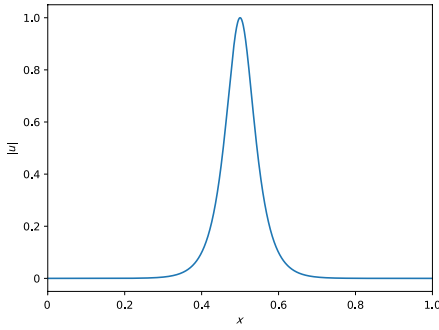
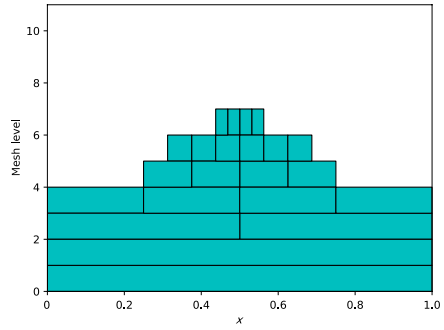
(a) Numerical solution at $t = 0$ (b) Active elements at $t = 0$ (c) Numerical solution at $t = 0.4$ (d) Active elements at $t = 0.4$ (e) Numerical solution at $t = 0.6$ (f) Active elements at $t = 0.6$

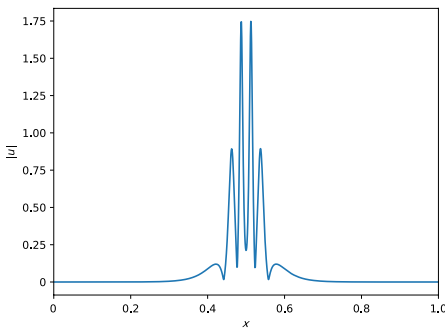
Fig. 6 Example 3: bound state solution of solitons with $L = 4$. Left: numerical solutions; right: active elements. $t = 0, 0.4$ and 0.6 . $N = 9$, $k = 3$, $\epsilon = 10^{-4}$ and $\eta = 10^{-5}$



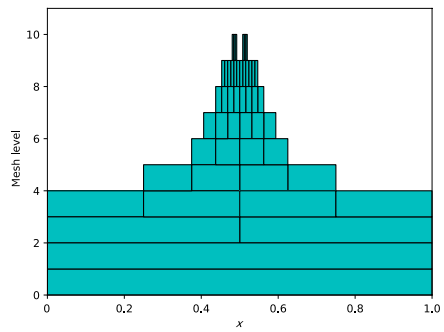
(a) Numerical solution at $t = 0$



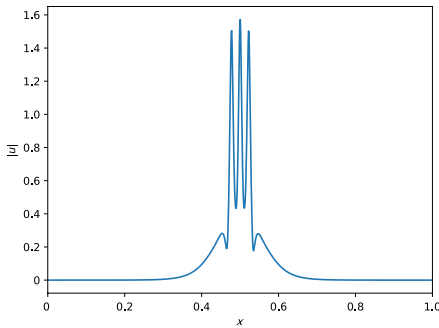
(b) Active elements at $t = 0$



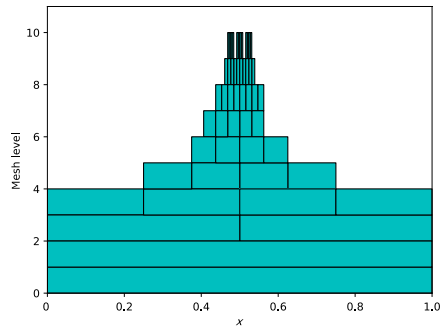
(c) Numerical solution at $t = 0.4$



(d) Active elements at $t = 0.4$



(e) Numerical solution at $t = 0.6$



(f) Active elements at $t = 0.6$

Fig. 7 Example 3: bound state solution of solitons with $L = 5$. Left: numerical solutions; right: active elements. $t = 0, 0.4$ and 0.6 . $N = 10, k = 3, \epsilon = 10^{-4}$ and $\eta = 10^{-5}$

Table 3 Example 4, accuracy test for the coupled NLS equation, $d = 1$. Adaptive. $t = 1$

	ϵ	DoF	Real part of u			Imaginary part of u		
			L^2 -error	R_{DoF}	R_ϵ	L^2 -error	R_{DoF}	R_ϵ
$k = 1$	1×10^{-1}	28	4.42×10^{-2}	–	–	5.49×10^{-2}	–	–
	1×10^{-2}	74	9.25×10^{-3}	1.61	0.68	1.43×10^{-2}	1.39	0.59
	1×10^{-3}	152	1.30×10^{-3}	2.72	0.85	2.04×10^{-3}	2.70	0.85
	1×10^{-4}	304	6.22×10^{-4}	1.07	0.32	1.05×10^{-3}	0.96	0.29
$k = 2$	1×10^{-1}	36	9.02×10^{-3}	–	–	1.12×10^{-2}	–	–
	1×10^{-2}	54	1.38×10^{-3}	4.62	0.81	1.59×10^{-3}	4.82	0.85
	1×10^{-3}	105	1.39×10^{-4}	3.45	1.00	1.68×10^{-4}	3.38	0.98
	1×10^{-4}	186	2.05×10^{-5}	3.35	0.83	1.99×10^{-5}	3.73	0.93
$k = 3$	1×10^{-1}	44	1.26×10^{-2}	–	–	1.69×10^{-2}	–	–
	1×10^{-2}	60	6.82×10^{-4}	9.40	1.27	1.21×10^{-3}	8.50	1.15
	1×10^{-3}	84	8.22×10^{-5}	6.29	0.92	1.28×10^{-4}	6.68	0.98
	1×10^{-4}	136	1.16×10^{-5}	4.06	0.85	1.75×10^{-5}	4.13	0.86

	ϵ	DoF	Real part of v			Imaginary part of v		
			L^2 -error	R_{DoF}	R_ϵ	L^2 -error	R_{DoF}	R_ϵ
$k = 1$	1×10^{-1}	28	1.13×10^{-1}	–	–	8.66×10^{-2}	–	–
	1×10^{-2}	74	2.75×10^{-2}	1.46	0.62	2.57×10^{-2}	1.25	0.53
	1×10^{-3}	152	4.60×10^{-3}	2.49	0.78	4.34×10^{-3}	2.47	0.77
	1×10^{-4}	304	1.97×10^{-3}	1.22	0.37	1.79×10^{-3}	1.28	0.38
$k = 2$	1×10^{-1}	36	2.07×10^{-2}	–	–	2.12×10^{-2}	–	–
	1×10^{-2}	54	3.56×10^{-3}	4.34	0.76	3.39×10^{-3}	4.52	0.80
	1×10^{-3}	105	3.27×10^{-4}	3.59	1.04	3.76×10^{-4}	3.31	0.95
	1×10^{-4}	186	4.82×10^{-5}	3.35	0.83	5.81×10^{-5}	3.27	0.81
$k = 3$	1×10^{-1}	44	2.81×10^{-2}	–	–	2.50×10^{-2}	–	–
	1×10^{-2}	60	1.44×10^{-3}	9.58	1.29	1.43×10^{-3}	9.24	1.24
	1×10^{-3}	84	1.49×10^{-4}	6.75	0.99	1.68×10^{-4}	6.36	0.93
	1×10^{-4}	136	2.16×10^{-5}	4.01	0.84	3.43×10^{-5}	3.30	0.69

$$\begin{cases} u(x, t) = \sqrt{\frac{2a}{1+\beta}} \operatorname{sech}\left(\sqrt{2a}(X - ct)\right) \exp\left(i\left((c - \alpha)X - \left(\frac{c^2 - a^2}{2} - a\right)t\right)\right), \\ v(x, t) = \sqrt{\frac{2a}{1+\beta}} \operatorname{sech}\left(\sqrt{2a}(X - ct)\right) \exp\left(i\left((c + \alpha)X - \left(\frac{c^2 - a^2}{2} - a\right)t\right)\right), \end{cases} \quad (19)$$

where $c = 1, a = 1, \alpha = \frac{1}{2}, \beta = \frac{2}{3}$ and $X = M(x - 0.5), M = 50$. The periodic boundary condition is applied in $[0, 1]$. The solutions are computed up to $t = 1$. We take $\Delta t = \frac{0.1M\Delta x}{\alpha}$, the maximum mesh level $N = 10$, and $\eta = \epsilon/10$. The accuracy results are shown in [Table 3](#). We can observe that the approximation with a higher polynomial degree outperforms that with a lower polynomial degree. Note that the method has saturated when $\epsilon = 10^{-4}$ for $k = 1$; therefore, the error does not decay too much.

Example 5 In this example, we consider the solitary wave propagation and soliton interaction for the coupled NLS equation (18) following [45]. In this example, $\Delta t = \frac{0.1M\Delta x}{\alpha}$.

We first take the initial condition for soliton propagation

$$\begin{cases} u(x, 0) = \sqrt{\frac{2\alpha}{1+\beta}} \operatorname{sech}(\sqrt{2\alpha}X) \exp(i(c - \alpha)X), \\ v(x, 0) = \sqrt{\frac{2\alpha}{1+\beta}} \operatorname{sech}(\sqrt{2\alpha}X) \exp(i(c + \alpha)X) \end{cases} \tag{20}$$

with the same parameters in Example 4 except $X = M(x - 0.2)$, $M = 100$. The periodic boundary condition is used in $[0, 1]$. The numerical solutions and active elements at $t = 0, 20$ and 50 are presented in Fig. 8. The plots of $|u|$ and $|v|$ are similar; thus, we only show the results of $|u|$ here.

For interaction of two solitons, we use the following initial condition:

$$\begin{cases} u(x, 0) = \sum_{j=1}^2 \sqrt{\frac{2a_j}{1+\beta}} \operatorname{sech}(\sqrt{2a_j}X_j) \exp(i(c_j - \alpha)X_j), \\ v(x, 0) = \sum_{j=1}^2 \sqrt{\frac{2a_j}{1+\beta}} \operatorname{sech}(\sqrt{2a_j}X_j) \exp(i(c_j + \alpha)X_j), \end{cases} \tag{21}$$

where $c_1 = 1, c_2 = 0.1, a_1 = 1, a_2 = 0.5, \alpha = \frac{1}{2}, \beta = \frac{2}{3}$ and $X_j = M(x - 0.2 - x_j)$, $M = 100, x_1 = 0, x_2 = 0.25$. The periodic boundary condition is used in $[0, 1]$. The numerical solutions of $|u|$ and active elements at $t = 0, 20$ and 50 are presented in Fig. 9. The interaction is elastic and the solitons restore their original shapes.

Next, we consider interaction of three solitons with initial condition

$$\begin{cases} u(x, 0) = \sum_{j=1}^3 \sqrt{\frac{2a_j}{1+\beta}} \operatorname{sech}(\sqrt{2a_j}X_j) \exp(i(c_j - \alpha)X_j), \\ v(x, 0) = \sum_{j=1}^3 \sqrt{\frac{2a_j}{1+\beta}} \operatorname{sech}(\sqrt{2a_j}X_j) \exp(i(c_j + \alpha)X_j), \end{cases} \tag{22}$$

where $c_1 = 1, c_2 = 0.1, c_3 = -1, a_1 = 1.2, a_2 = 0.72, a_3 = 0.36, \alpha = \frac{1}{2}, \beta = \frac{2}{3}$ and $X_j = M(x - 0.2 - x_j)$, $M = 100, x_1 = 0, x_2 = 0.25, x_3 = 0.5$. The periodic boundary condition is used in $[0, 1]$. The numerical solutions of $|u|$ and active elements at $t = 0, 20$ and 50 are presented in Fig. 10. Notice that the three solitons restore their original shapes after the interaction.

4.4 NLS Equation in 2D

Example 6 In this example, we consider the singular solutions for the 2D NLS equation

$$iu_t + \frac{1}{M^2}u_{xx} + \frac{1}{M^2}u_{yy} + |u|^2u = 0 \tag{23}$$

with the initial condition [45]

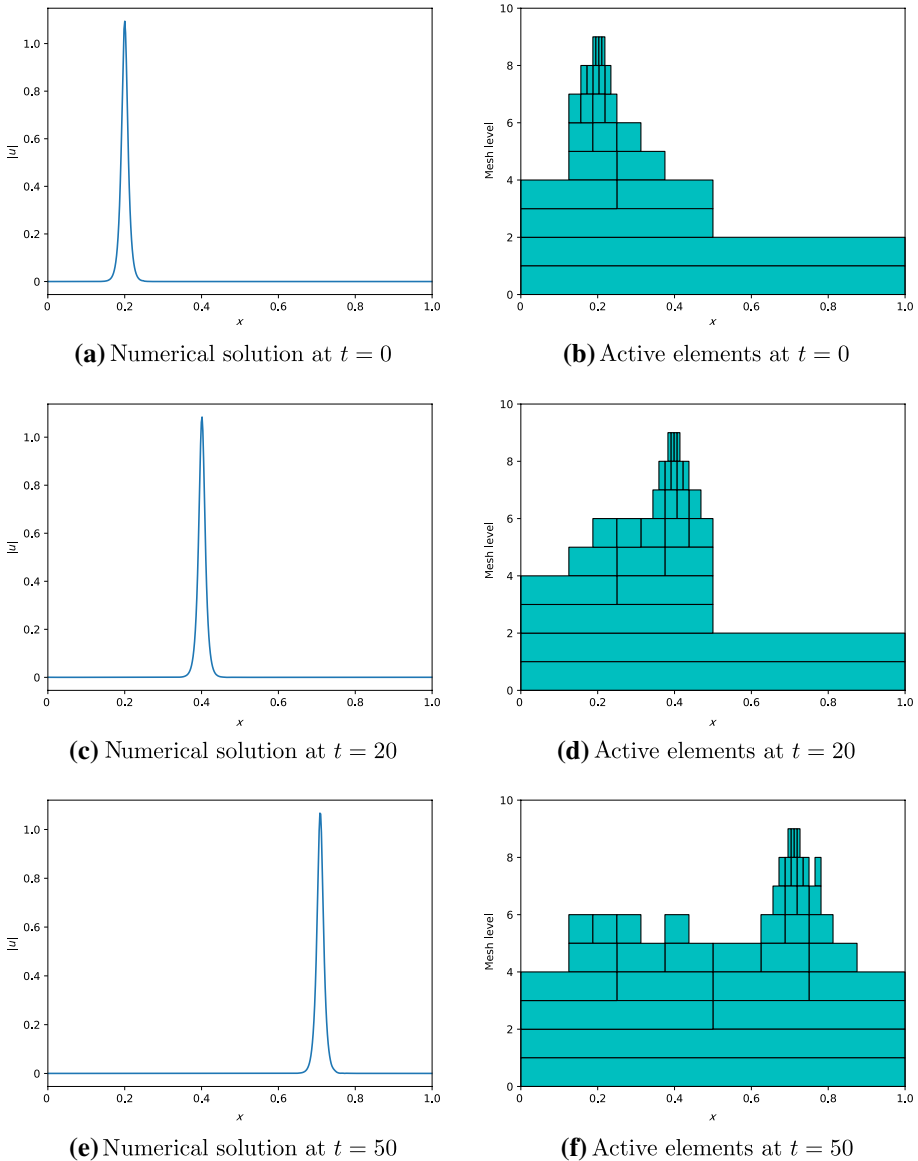
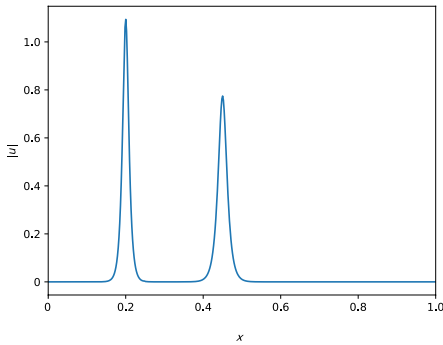


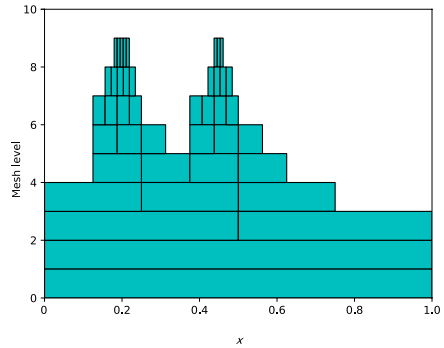
Fig. 8 Example 5: coupled NLS equation, single soliton. Left: numerical solutions; right: active elements. $t = 0, 20$ and 50 . $N = 9, k = 3, \epsilon = 10^{-4}$ and $\eta = 5 \times 10^{-5}$

$$u(x, 0) = (1 + \sin X)(2 + \sin Y) \tag{24}$$

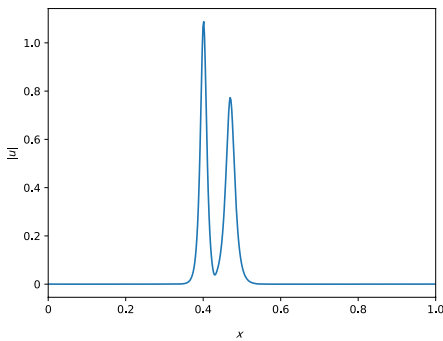
where $X = Mx, Y = My, M = 2\pi$. Periodic boundary conditions are applied in $[0, 1]^2$. Strong evidence of a singularity in finite time is obtained. The plots of $|u|$ and active elements at $t = 0$ and $t = 0.108$ are shown in Fig. 11. From the results, we can observe that a singular is generated at $t = 0.108$ and our method can capture the structure adaptively.



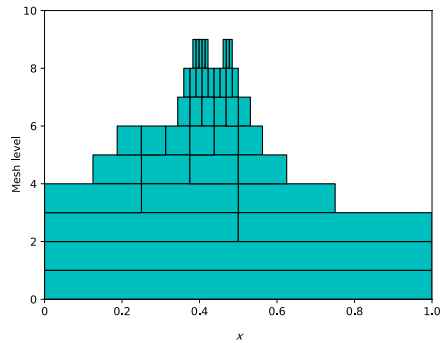
(a) Numerical solution at $t = 0$



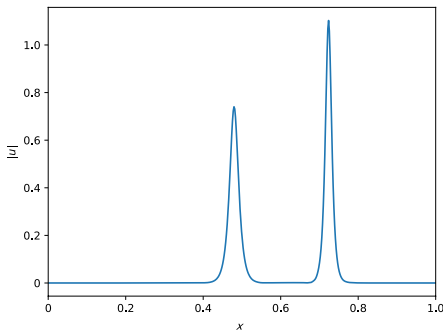
(b) Active elements at $t = 0$



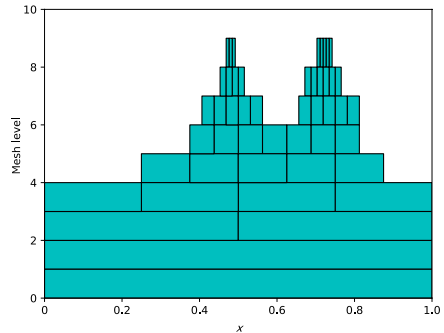
(c) Numerical solution at $t = 20$



(d) Active elements at $t = 20$



(e) Numerical solution at $t = 50$



(f) Active elements at $t = 50$

Fig. 9 Example 5: coupled NLS equation, double solitons. Left: numerical solutions; right: active elements. $t = 0, 20$ and 50 . $N = 9, k = 3, \epsilon = 10^{-4}$ and $\eta = 4 \times 10^{-5}$

Example 7 In this example, we consider the 2D NLS equation (23) with the initial condition [46]

$$u(x, 0) = 2.0 + 0.01 \sin\left(X + \frac{\pi}{4}\right) \sin\left(Y + \frac{\pi}{4}\right), \tag{25}$$

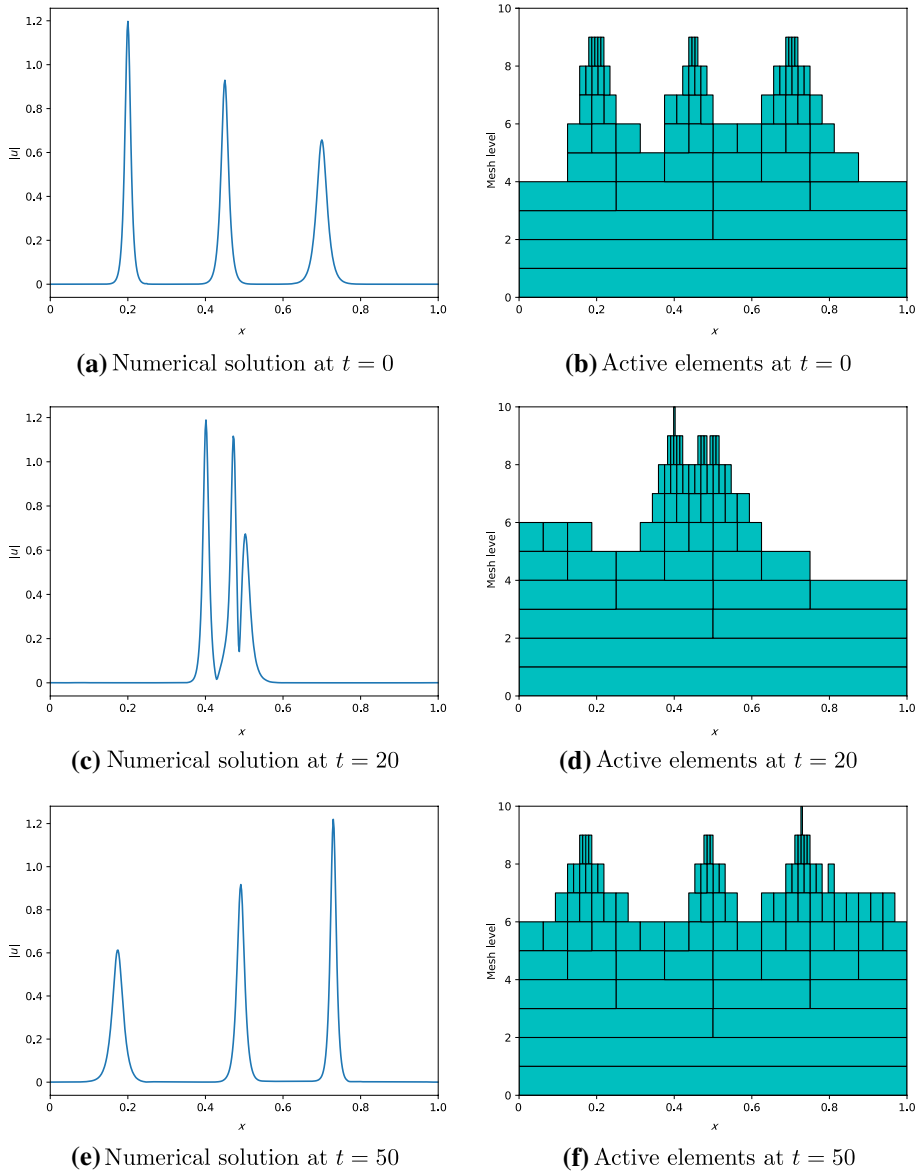


Fig. 10 Example 5: coupled NLS equation, triple solitons. Left: numerical solutions; right: active elements. $t = 0, 20$ and 50 . $N = 9, k = 3, e = 10^{-4}$ and $\eta = 4 \times 10^{-5}$

where $X = M(x - 0.5), Y = M(y - 0.5), M = 2\pi$. Periodic boundary conditions are applied in $[0, 1]^2$. The plots of $|u|$ and active elements at $t = 0$ and $t = 1.5813$ are shown in Fig. 12. We can observe the blow-up phenomenon in $|u|$ at $t = 1.5813$.

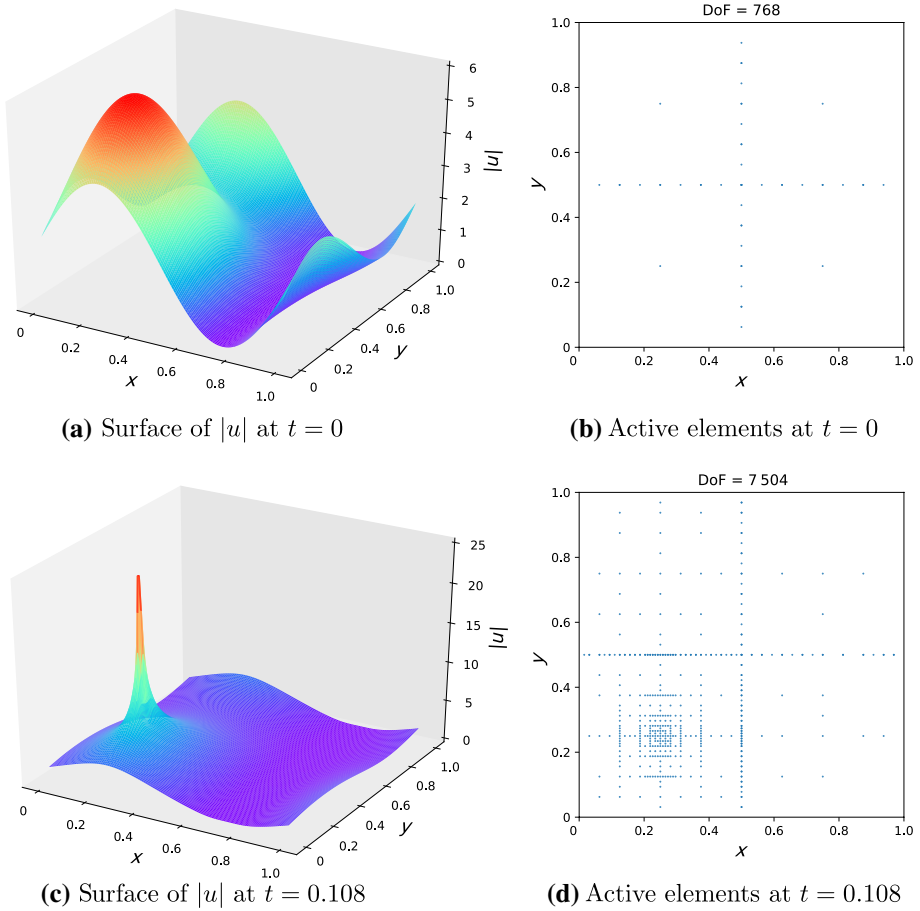


Fig. 11 Example 6: singular solutions in 2D NLS equation. Left: numerical solutions; right: active elements. $t = 0$ and 0.108 . $N = 7, k = 3, \epsilon = 10^{-4}$ and $\eta = 10^{-5}$

Example 8 In this example, we consider the 2D NLS equation (23) with the initial condition [47]

$$u(x, 0) = 6\sqrt{2} \exp(-X^2 - Y^2), \tag{26}$$

where $X = M(x - 0.5)$, $Y = M(y - 0.5)$ and $M = 10$. Periodic boundary conditions are applied in $[0, 1]^2$. The plots of $|u|$ and active elements at $t = 0$ and $t = 0.04$ are shown

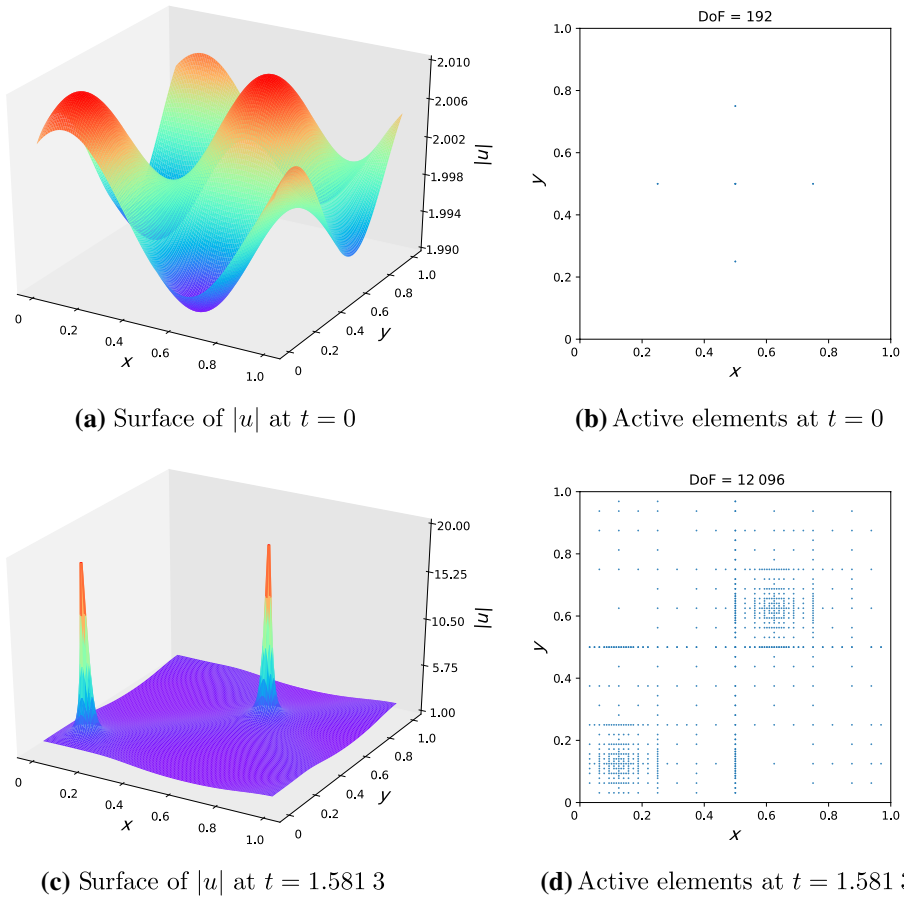
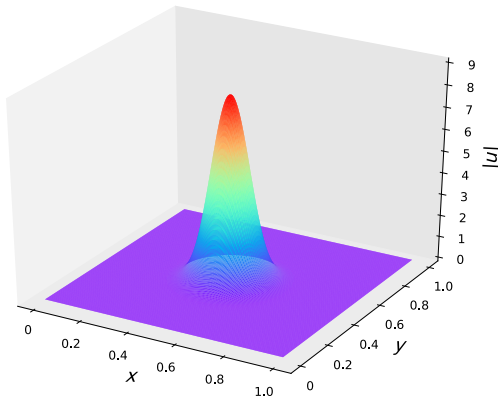


Fig. 12 Example 7: blow-up solution in 2D NLS equation. Left: numerical solutions; right: active elements. $t = 0$ and 1.5813 . $N = 7, k = 3, \epsilon = 10^{-4}$ and $\eta = 10^{-5}$

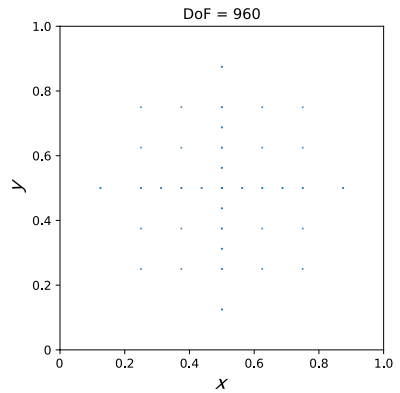
in Fig. 13. We observe from the results that the solution blows up in the center and our method can capture the blow-up phenomenon.

5 Conclusion

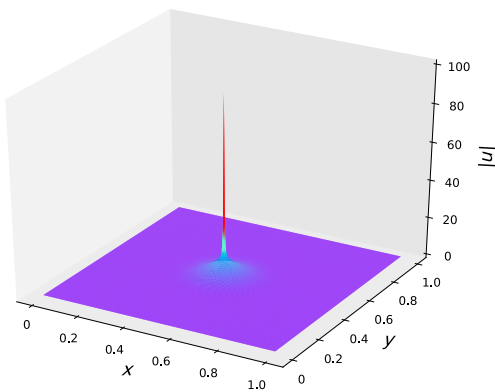
In this paper, we propose an adaptive multiresolution ultra-weak DG method to solve nonlinear Schrödinger equations. The adaptive multiwavelets are applied to achieve the multiresolution. The Alpert's multiwavelets are used to express the DG solution and the interpolatory multiwavelets are exploited to compute the nonlinear source term. Various numerical experiments are presented to demonstrate the excellent capability



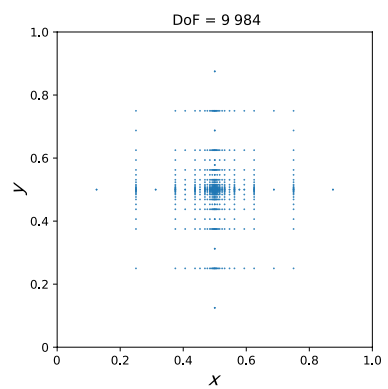
(a) Surface of $|u|$ at $t = 0$



(b) Active elements at $t = 0$



(c) Surface of $|u|$ at $t = 0.04$



(d) Active elements at $t = 0.04$

Fig. 13 Example 8: single blow-up solution in 2D NLS equation. Left: numerical solutions; right: active elements. $t = 0$ and 0.04 . $N = 9, k = 3, \epsilon = 10^{-3}$ and $\eta = 10^{-4}$

of capturing the soliton waves and the blow-up phenomenon. The code generating the results in this paper can be found at the GitHub link: <https://github.com/JuntaoHuang/adaptive-multiresolution-DG>.

Acknowledgements We would like to thank Qi Tang and Kai Huang for the assistance and discussion in code implementation.

Funding Y. Liu: Research supported in part by a grant from the Simons Foundation (426993, Yuan Liu). W. Guo: Research is supported by NSF grant DMS-1830838. Y. Cheng: Research is supported by NSF grants DMS-1453661 and DMS-1720023. Z. Tao: Research is supported by NSFC Grant 12001231.

Compliance with ethical standards

Conflicts of interest On behalf of all authors, the corresponding author states that there is no conflict of interest.

References

1. Alpert, B.K.: A class of bases in L^2 for the sparse representation of integral operators. *SIAM J. Math. Anal.* **24**(1), 246–262 (1993)
2. Berger, M.J., Colella, P.: Local adaptive mesh refinement for shock hydrodynamics. *J. Comput. Phys.* **82**(1), 64–84 (1989)
3. Bungartz, H.-J., Griebel, M.: Sparse grids. *Acta Numerica* **13**(1), 147–269 (2004)
4. Burstedde, C., Wilcox, L.C., Ghattas, O.: p4est: Scalable algorithms for parallel adaptive mesh refinement on forests of octrees. *SIAM J. Sci. Comput.* **33**(3), 1103–1133 (2011)
5. Chang, Q., Jia, E., Sun, W.: Difference schemes for solving the generalized nonlinear Schrödinger equation. *J. Comput. Phys.* **148**(2), 397–415 (1999)
6. Chang, Q., Wang, G.: Multigrid and adaptive algorithm for solving the nonlinear Schrödinger equation. *J. Comput. Phys.* **88**(2), 362–380 (1990)
7. Chen, A., Cheng, Y., Liu, Y., Zhang, M.: Superconvergence of ultra-weak discontinuous Galerkin methods for the linear Schrödinger equation in one dimension. *J. Sci. Comput.* **82**(1), 1–44 (2020)
8. Chen, A., Li, F., Cheng, Y.: An ultra-weak discontinuous Galerkin method for Schrödinger equation in one dimension. *J. Sci. Comput.* **78**(2), 772–815 (2019)
9. Cheng, Y., Shu, C.-W.: A discontinuous Galerkin finite element method for time dependent partial differential equations with higher order derivatives. *Math. Comput.* **77**(262), 699–730 (2008)
10. Chiao, R.Y., Garmire, E., Townes, C.H.: Self-trapping of optical beams. *Phys. Rev. Lett.* **13**(15), 479–482 (1964)
11. Cockburn, B., Hou, S., Shu, C.-W.: The Runge-Kutta local projection discontinuous Galerkin finite element method for conservation laws. IV. The multidimensional case. *Math. Comput.* **54**(190), 545–581 (1990)
12. Cockburn, B., Karniadakis, G. E., Shu, C.-W.: The development of discontinuous Galerkin methods. In: Cockburn, B., Karniadakis, G.E., Shu, C.-W. (eds). *Discontinuous Galerkin Methods. Lecture Notes in Computational Science and Engineering*, vol. 11, pp. 3–50. Springer, Berlin, Heidelberg (2000)
13. Cockburn, B., Shu, C.-W.: Runge-Kutta discontinuous Galerkin methods for convection-dominated problems. *J. Sci. Comput.* **16**(3), 173–261 (2001)
14. De la Hoz, F., Vadiillo, F.: An exponential time differencing method for the nonlinear Schrödinger equation. *Comput. Phys. Commun.* **179**(7), 449–456 (2008)
15. Gerhard, N., Müller, S.: Adaptive multiresolution discontinuous Galerkin schemes for conservation laws: multi-dimensional case. *Comput. Appl. Math.* **35**(2), 321–349 (2016)
16. Griffiths, D.F., Mitchell, A.R., Morris, J.L.: A numerical study of the nonlinear Schrödinger equation. *Comput. Methods Appl. Mechan. Eng.* **45**, 177–215 (1984)
17. Guo, L., Xu, Y.: Energy conserving local discontinuous Galerkin methods for the nonlinear Schrödinger equation with wave operator. *J. Sci. Comput.* **65**(2), 622–647 (2015)
18. Guo, W., Cheng, Y.: A sparse grid discontinuous Galerkin method for high-dimensional transport equations and its application to kinetic simulations. *SIAM J. Sci. Comput.* **38**(6), A3381–A3409 (2016)
19. Guo, W., Cheng, Y.: An adaptive multiresolution discontinuous Galerkin method for time-dependent transport equations in multidimensions. *SIAM J. Sci. Comput.* **39**(6), A2962–A2992 (2017)
20. Guo, W., Huang, J., Tao, Z., Cheng, Y.: An adaptive sparse grid local discontinuous Galerkin method for Hamilton-Jacobi equations in high dimensions. [arXiv: 2006.05250](https://arxiv.org/abs/2006.05250) (2020)
21. Huang, J., Cheng, Y.: An adaptive multiresolution discontinuous Galerkin method with artificial viscosity for scalar hyperbolic conservation laws in multidimensions. [arXiv: 1906.00829](https://arxiv.org/abs/1906.00829) (2019)
22. Huang, J., Liu, Y., Guo, W., Tao, Z., Cheng, Y.: An adaptive multiresolution interior penalty discontinuous Galerkin method for wave equations in second order form. [arXiv: 2004.08525](https://arxiv.org/abs/2004.08525) (2020)
23. Huang, J., Shu, C.-W.: Error estimates to smooth solutions of semi-discrete discontinuous Galerkin methods with quadrature rules for scalar conservation laws. *Numer. Methods Part. Differ. Equ.* **33**(2), 467–488 (2017)
24. Ismail, M., Taha, T.R.: Numerical simulation of coupled nonlinear Schrödinger equation. *Math. Comput. Simul.* **56**(6), 547–562 (2001)
25. Karakashian, O., Makridakis, C.: A space-time finite element method for the nonlinear Schrödinger equation: the discontinuous Galerkin method. *Math. Comput.* **67**(222), 479–499 (1998)
26. Kormann, K.: A time-space adaptive method for the Schrödinger equation. *Commun. Comput. Phys.* **20**(1), 60–85 (2016)

27. Liang, X., Khaliq, A.Q.M., Xing, Y.: Fourth order exponential time differencing method with local discontinuous Galerkin approximation for coupled nonlinear Schrödinger equations. *Commun. Comput. Phys.* **17**(2), 510–541 (2015)
28. Liu, H., Huang, Y., Lu, W., Yi, N.: On accuracy of the mass-preserving DG method to multi-dimensional Schrödinger equations. *IMA J. Numer. Anal.* **39**(2), 760–791 (2019)
29. Lu, W., Huang, Y., Liu, H.: Mass preserving discontinuous Galerkin methods for Schrödinger equations. *J. Comput. Phys.* **282**, 210–226 (2015)
30. Mallat, S.: *A Wavelet Tour of Signal Processing*. Elsevier, Amsterdam (1999)
31. Miles, J.W.: An envelope soliton problem. *SIAM J. Appl. Math.* **41**(2), 227–230 (1981)
32. Newell, A.C.: *Solitons in Mathematics and Physics*. SIAM, Philadelphia (1985)
33. Pareschi, L., Russo, G.: Implicit-explicit Runge-Kutta schemes and applications to hyperbolic systems with relaxation. *J. Sci. Comput.* **25**(1), 129–155 (2005)
34. Pathria, D., Morris, J.L.: Pseudo-spectral solution of nonlinear Schrödinger equations. *J. Comput. Phys.* **87**(1), 108–125 (1990)
35. Reed, W.H., Hill, T.R.: *Triangular mesh methods for the neutron transport equation*. Technical report, Los Alamos: Scientific Lab, USA (1973)
36. Sanz-Serna, J., Verwer, J.: Conservative and nonconservative schemes for the solution of the nonlinear Schrödinger equation. *IMA J. Numer. Anal.* **6**(1), 25–42 (1986)
37. Sanz-Serna, J.M., Christie, I.: A simple adaptive technique for nonlinear wave problems. *J. Comput. Phys.* **67**(2), 348–360 (1986)
38. Sheng, Q., Khaliq, A., Al-Said, E.: Solving the generalized nonlinear Schrödinger equation via quartic spline approximation. *J. Comput. Phys.* **166**(2), 400–417 (2001)
39. Sulem, P., Sulem, C., Patera, A.: Numerical simulation of singular solutions to the two-dimensional cubic Schrödinger equation. *Commun. Pure Appl. Math.* **37**(6), 755–778 (1984)
40. Taha, T.R., Ablowitz, M.I.: Analytical and numerical aspects of certain nonlinear evolution equations. II. Numerical, nonlinear Schrödinger equation. *J. Comput. Phys.* **55**(2), 203–230 (1984)
41. Tao, Z.J., Jiang Y., Cheng Y.D.: An adaptive high-order piecewise polynomial based sparse grid collocation method with applications. [arXiv: 1912.03982](https://arxiv.org/abs/1912.03982) (2019)
42. Wang, Z., Tang, Q., Guo, W., Cheng, Y.: Sparse grid discontinuous Galerkin methods for high-dimensional elliptic equations. *J. Comput. Phys.* **314**, 244–263 (2016)
43. Whitham, G.B.: *Linear and Nonlinear Waves*. John Wiley and Sons, New York (2011)
44. Xiong, C., Luo, F., Ma, X.: Uniform in time error analysis of HDG approximation for Schrödinger equation based on HDG projection. *ESAIM Math. Modell. Numer. Anal.* **52**(2), 751–772 (2018)
45. Xu, Y., Shu, C.-W.: Local discontinuous Galerkin methods for nonlinear Schrödinger equations. *J. Comput. Phys.* **205**(1), 72–97 (2005)
46. Zhang, R.: Compact implicit integration factor methods for some complex-valued nonlinear equations. *Chinese Phys. B* **21**(4), 040205 (2012)
47. Zhang, R., Yu, X., Li, M., Li, X.: A conservative local discontinuous Galerkin method for the solution of nonlinear Schrödinger equation in two dimensions. *Sci. China Math.* **60**(12), 2515–2530 (2017)